Nanoscale

PAPER

View Article Online
View Journal | View Issue

Cite this: *Nanoscale*, 2025, **17**, 25325

Atomistic observation of defect evolution during solidification in semiconductor InAs

Changxin Han, [a] Bohua Zhang,[a] He Zheng[b] and Scott X. Mao*[a,b]

Received 29th June 2025,
Accepted 3rd October 2025

DOI: 10.1039/d5nr02745d

rsc.li/nanoscale

The structural and phase stability of semiconductors has attracted considerable attention due to their potential applications in next-generation optoelectronic, thermoelectric, and quantum devices. Atomistic observations are crucial for understanding the defect formation during solidification in semiconductors. In this study, an *in situ* biasing experiment was conducted using a transmission electron microscope to investigate the detailed evolution of stacking faults and twinning at the solid–liquid interface in InAs. The results highlight that nucleation energy regulation is key to defect formation. Additionally, thermally driven dislocation slip, stacking fault dynamics, and twin dissociation reveal new pathways for defect evolution in advanced semiconductors.

1. Introduction

The structural and phase stability of semiconductors has gained significant attention due to their potential applications in next-generation optoelectronic, thermoelectric, and quantum devices.[1–4] Among these materials, indium arsenide (InAs) is particularly noteworthy for excellent physical properties, including a narrow direct bandgap (0.35 eV), high electron mobility, and strong quantum confinement effects.[5–7] These characteristics make InAs an ideal candidate for infrared photodetectors, field-effect transistors (FETs), and quantum transport applications.[8–15]

A unique feature of III–V semiconductors, including InAs, is their ability to crystallize in two distinct polymorphic phases: the metastable wurtzite (WZ) phase with a hexagonal crystal structure and the thermodynamically stable zinc blende (ZB) phase with a cubic crystal structure.[12,16–19] The coexistence of these phases often leads to the formation of stacking faults, twin boundaries, and other planar defects along the growth axis, which can significantly influence their physical properties.[20–23] In particular, the introduction of twin boundaries can result in a periodic arrangement known as a twin superlattice, where atomic-scale twin boundaries alternate periodically within the crystal lattice.[24,25] These twin superlattices are of great interest because they can modify the electronic band structure, tune charge carrier mobility, and enhance mechanical strength in semiconductor nanowires.[26–29]

The properties of InAs are highly sensitive to defect populations, yet the mechanisms underpinning their evolution during growth through solidification remain to be elucidated. The formation of defects is believed to occur through the nucleation and migration of atomic planes, often driven by thermal or mechanical perturbations.[30] However, understanding the defect formation mechanism through capturing these dynamic processes with sufficient temporal and spatial resolution has proven challenging. Conventional *ex situ* characterization methods, such as X-ray diffraction or *ex situ* TEM, cannot provide atomically resolved defect formation during dynamic solidification, limiting our understanding of the structural evolution at the atomic scale.[27,31]

To address these challenges, *in situ* transmission electron microscopy (TEM) has emerged as a powerful method for probing dynamic structural transformations in nanomaterials. *In situ* TEM enables real-time atomic-scale imaging of phase transitions, defect dynamics, and growth mechanisms under controlled stimuli such as heating, stress, or electrical bias.[32–34] Recent studies utilizing *in situ* TEM have provided insights into growth in other III–V semiconductors, such as GaAs and InP, revealing the role of twin boundaries, interface energetics, and growth kinetics in dictating their structural evolution.[22,35–39] These studies underscore the importance of interfacial energetics in driving the periodicity and stability of twinning. However, direct atomic-scale observations of solidification and the associated evolution of defects remain limited.

Herein, we employed *in situ* high-resolution TEM (HRTEM) to investigate the atomic resolved defect dynamic evolution in InAs. By the "come and go" process of solidification and liquefaction of InAs, we observe the dynamic processes that take place during solidification for stacking faults and twinning. These findings not only provide fundamental insights into the

[a]*School of Materials Engineering, Purdue University, West Lafayette, IN 47907, USA. E-mail: mao217@purdue.edu*
[b]*Department of Mechanical Engineering and Materials Science, University of Pittsburgh, Pittsburgh, PA 15261, USA*

structural stability in III–V semiconductors but also offer a basis for controlling stacking faults and twinning during solidification in nanoscale materials. Such defect-controlled architectures hold great promise for optimizing the electronic and mechanical properties of next generation semiconductors, enabling their tailored use in advanced device applications.

2. Methods

The InAs was synthesized using metal–organic vapor phase epitaxy (MOVPE) *via* the vapor–liquid–solid (VLS) mechanism. The VLS growth process for InAs has been comprehensively investigated.[40] InAs (111)B substrates were solvent-cleaned; Au nanoparticles (~40 nm, ~0.3 μm^{-2}) were deposited as catalysts. For growth, TMIn (In precursor) and AsH_3 (As precursor) were used in the H_2 carrier at ~100 Torr in a horizontal OMVPE reactor. Substrates were ramped to 450–540 °C and stabilized for 2–5 min; TMIn was introduced for 5–8 min while AsH_3 was maintained during ramp, growth, and cool-down. The inlet V/III (AsH_3/TMIn molar) was set between ~10 and 100 to balance VLS yield *vs.* VS deposition. After growth, TMIn was closed first and AsH_3 held during cool-down to suppress As loss; the samples were then removed for an *in situ* TEM experiment.

The experiment was performed inside an FEI Tecnai F30 field-emission gun TEM operated at 300 kV. Employing the Nanofactory TEM-STM platform,[41–43] a single InAs nanowire which grows on the GaAs substrate is Joule heated by passing a current through it using the etched gold tip (Fig. 1). Unlike its bulk counterpart which exhibits the ZB structure, the InAs grown *via* this method predominantly adopts a WZ structure ($a = b = 4.30$ Å, $c = 7.04$ Å), consistent with the previous experimental observation.[6] After approaching the gold tip until it made good contact with the nanowire, we started heating the InAs nanowire by slowly increasing the DC voltage and thus the DC current until the AuIn began to melt. For other experimental details, please refer to our previously published paper.[6]

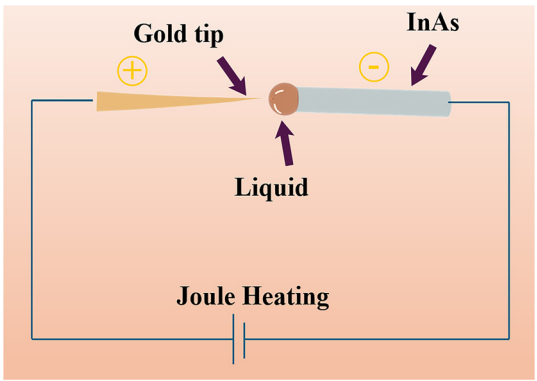

Fig. 1 Schematic diagram of the experimental setup.

3. Results

3.1. Solidification without planar defects

Nanoscale InAs with the designed solid–liquid interface provides a model system to study the dynamic crystalline evolution during the solidification and liquefaction period. Fig. 2 illustrates the solidification process of a planar defect-free InAs, where the contact angle (CA) at the solid–liquid interface remains at nearly 90 degrees, ensuring stable and coherent layer-by-layer growth.

In Fig. 2a, the early stage of InAs formation shows a smooth and continuous interface, with the absence of defects. This suggests that the solidification front remains well-ordered, facilitated by an equilibrium configuration that balances interfacial energies between the liquid AuIn and solid InAs.[44] Besides, the ordered atomic layers of the {111} planes in Fig. 2b become apparent, reinforcing the role of the near-perpendicular CA in promoting epitaxial solidification along low-energy planes. Continuing this trend, Fig. 2c highlights the sustained progression of the planar defect-free InAs, where the interface retains its smooth and well-ordered morphology. Additionally, the near 90 degrees CA prevents excessive curvature effects that could introduce localized strain variations, which in turn suppress defect generation.[45,46] In the final stage, Fig. 2d suggests that the energetic landscape at the solidification front remains stable, allowing the phase solidification to proceed without irregularities. The well-faceted atomic planes indicate that solidification occurs in a controlled step-flow mode, where adatoms selectively attach to preferred lattice sites, thereby maintaining structural integrity.[47]

3.2. Defect generation during solidification

Fig. 3 shows the cyclic solidification and liquefaction of InAs, where two successive cycles are observed, each marked by distinct contact angles (CAs) and defect evolution. The first cycle, shown in Fig. 3a–c, exhibits a CA of approximately 75°, while the second cycle, illustrated in Fig. 3d–f, proceeds with a reduced CA of 43°. In both cycles, solidification and liquefaction occur simultaneously, driven by interfacial strain and atomic rearrangements at the solid–liquid interface. A key difference between the two cycles is the defect density: more stacking faults form in the second cycle than in the first, indicating a progressive accumulation of structural disorder as solidification advances.

The initial stage of the first cycle in Fig. 3a displays a well-ordered crystalline structure with minimal defect formation. The solid–liquid interface maintains a relatively smooth geometry, allowing for a controlled solidification process. With the progress of the system as shown in Fig. 3b, the onset of stacking fault emission becomes evident, as indicated by the small green arrows, facilitating strain relaxation within the solidified InAs.[48] Specifically, a Shockley partial is emitted from the interface, relieving the interfacial shear concentrated at a step/ledge. Subsequently, as shown in Fig. 3c, liquefaction and solidification proceed simultaneously, with the liquid phase advancing along the interface while the newly formed atomic layers integrate into the lattice. The red arrow high-

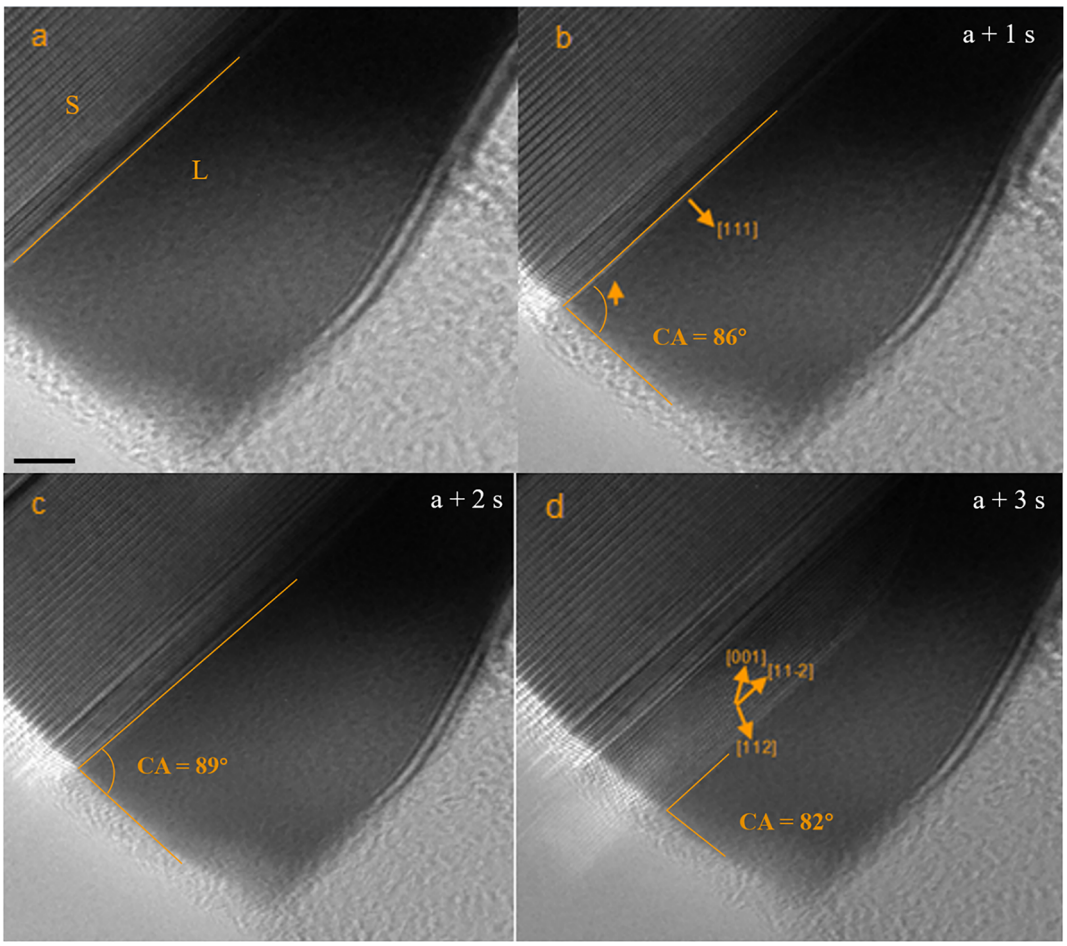

Fig. 2 Planar defect-free InAs solidification. (a) Sharp solid–liquid interface at the onset of transition. Orange line indicates the solid–liquid interface. (b) Nucleation of InAs with atomic planes along the [111] orientation. (c) Expansion of nanowires with an 89 degrees CA. (d) Growth of planar defect-free nanowires. Orientations: [001], [112], and [11–2]. Scale bar: 5 nm.

lights the direction of liquid transport, while the orange arrows trace the propagation of the liquefaction process. The CA of 75 degrees at this stage ensures moderate interfacial stability, supporting defect-limited growth.

In contrast, the second cycle, captured in Fig. 3d–f, follows a similar liquefaction and solidification sequence but with distinct structural differences. Specifically, in Fig. 3d, the solid–liquid interface becomes more irregular compared to that in the first cycle. As solidification progresses, as shown in Fig. 3e, a higher density of stacking faults appears, disrupting the uniformity of atomic layer incorporation. In Fig. 3f, the crystal undergoes further reorganization, with stacking faults propagating throughout the structure, as indicated by the green arrows. The reduced CA in this cycle suggests a shift in the interfacial energy balance, leading to increased atomic disorder and a higher likelihood of defect-mediated structural transformations.

3.3. Twinning superlattice formation during oscillatory solidification

Fig. 4 presents the solidification and liquefaction processes of the twin superlattice in InAs, illustrating the role of defect formation and evolution dynamics. Fig. 4(a–c) depict the solidification process, during which the solid–liquid CA progressively decreases, leading to an increase in defect formation. The green arrows highlight stacking faults, which appear as the solidification front advances. As structural strain accumulates, twin boundaries form, particularly evident in Fig. 4c, marking a critical transition in the structural dynamics. In contrast, Fig. 4(d–f) illustrate the subsequent liquefaction process, where the twin superlattice breaks down as thermal energy destabilizes the atomic lattice. The sequence of liquefaction follows a defect-mediated pathway, with stacking faults and twin boundaries acting as initiation sites for atomic diffusion and phase dissolution.

In the initial solidification stage, Fig. 4a shows a relatively stable solid–liquid interface with minimal structural distortions. The interface maintains a moderate CA, ensuring a steady attachment of atomic layers without significant stacking faults. However, as solidification progresses, as shown in Fig. 4b, stacking faults emerge with a decreased CA of 60 degrees. This stacking fault formation is attributed to the decreasing solid–liquid CA, which alters the solidification

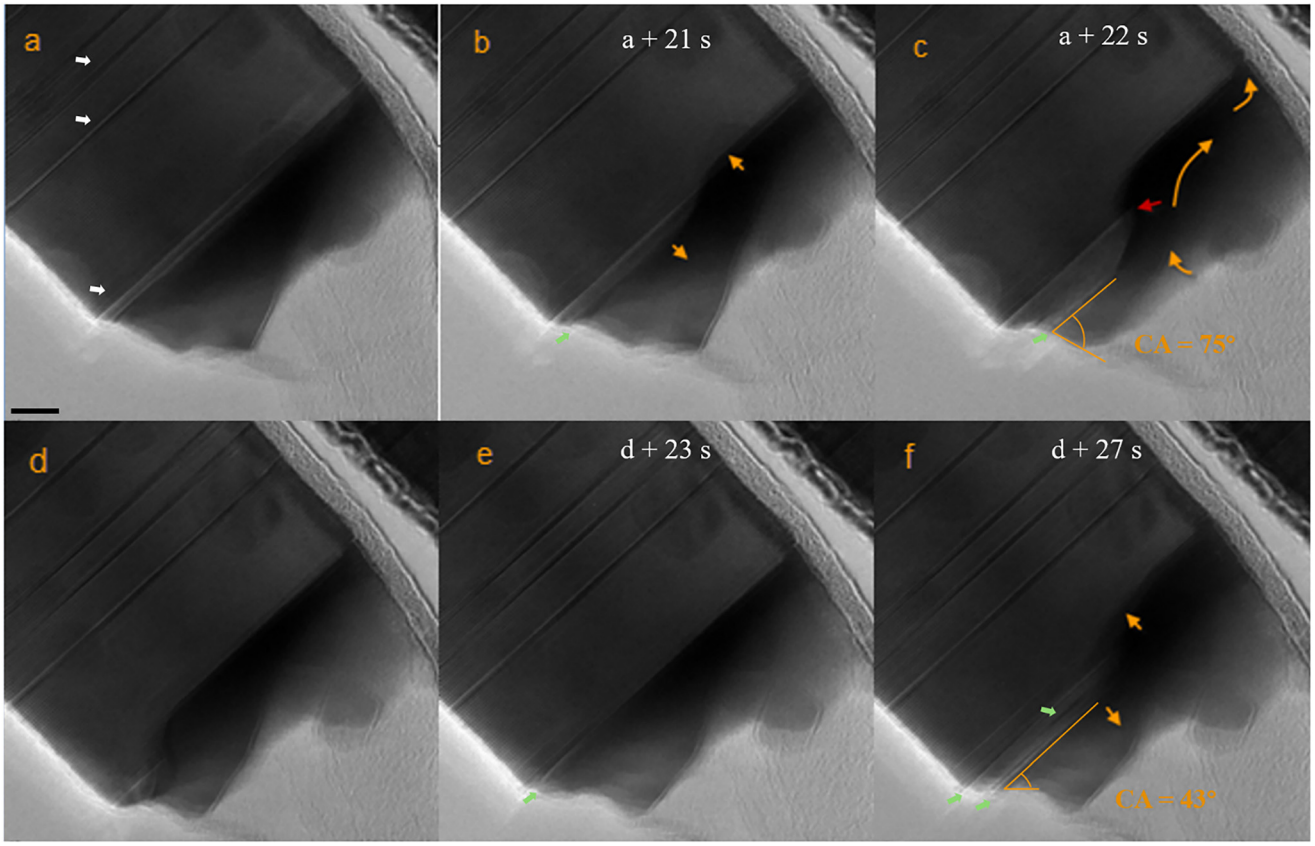

Fig. 3 Two cycles of oscillatory solidification and liquefaction. (a)–(c) indicate the first cycle with a CA of 75 degrees, (d) and (e) indicate the second cycle with a CA of 43 degrees. White arrows indicate the pristine stacking faults. Green arrows indicate the newly formed stacking faults. (a) Initial InAs with pristine stacking faults. (b) Nucleation of stacking faults near the solid–liquid interface. Orange arrows indicate the direction of solidification and liquefaction. (c) Propagation of InAs. Red arrow and orange arrows indicate the direction of the liquid flow. (d) Dissolution of InAs. (e) Nucleation of new stacking faults near the interface. (f) Propagation and formation of stacking faults. Scale bar: 10 nm.

kinetics and promotes crystallographic misalignment. As structural disorder increases, InAs undergoes a shift in its defect formation mechanisms.[49] In Fig. 4c, twin structures become clearly visible within InAs. The increasing density of stacking faults, combined with a further reduction in the CA (29 degrees), encourages the nucleation of twin boundaries.

As the liquid AuIn is exhausted, the solidification of InAs ends and enters the liquefaction stage. At this time, the liquefaction direction is perpendicular to the solidification direction, as shown in Fig. 4d–f. In Fig. 4d, the onset of liquefaction is observed at defect-rich regions where atomic distortions are most pronounced. The interface roughens as atomic diffusion increases, particularly along stacking faults and twin planes, which act as preferred pathways for disintegration. The dashed orange lines highlight the melting front, which progresses along structurally weaker areas of the lattice. As liquefaction advances in Fig. 4e, the solid–liquid interface becomes increasingly irregular, and atomic planes lose their ordered structure. At this stage, the transition from a crystalline to an amorphous-like phase begins, emphasizing the thermodynamic instability introduced by defect-mediated diffusion. The marked separation between the solid (S) and liquid (L) phases, as labeled, indicates that liquefaction proceeds in a well-defined direction, governed by defect distribution and strain energy minimization. Finally, in Fig. 4f, the complete phase breakdown is evident, with the twin superlattice transitioning into a disordered, amorphous-like liquid state. The twin boundaries that initially stabilized the solidification process now serve as preferential liquefaction pathways, guiding the collapse of lattice periodicity. The crystallographic orientations, labeled as {111} planes, suggest that liquefaction proceeds perpendicular to the twin superlattice growth direction, following the thermodynamically favorable route of strain energy minimization.[50] The liquid phase expands as the solid lattice disintegrates, driven by defect-assisted diffusion.

4. Discussion

4.1. Formation of stacking faults and twinning

To better understand the formation mechanism of stacking faults and twinning observed in the experiment in more detail, we introduce nucleation theory to provide a framework for its explanation. Nucleation plays a fundamental role in the VLS

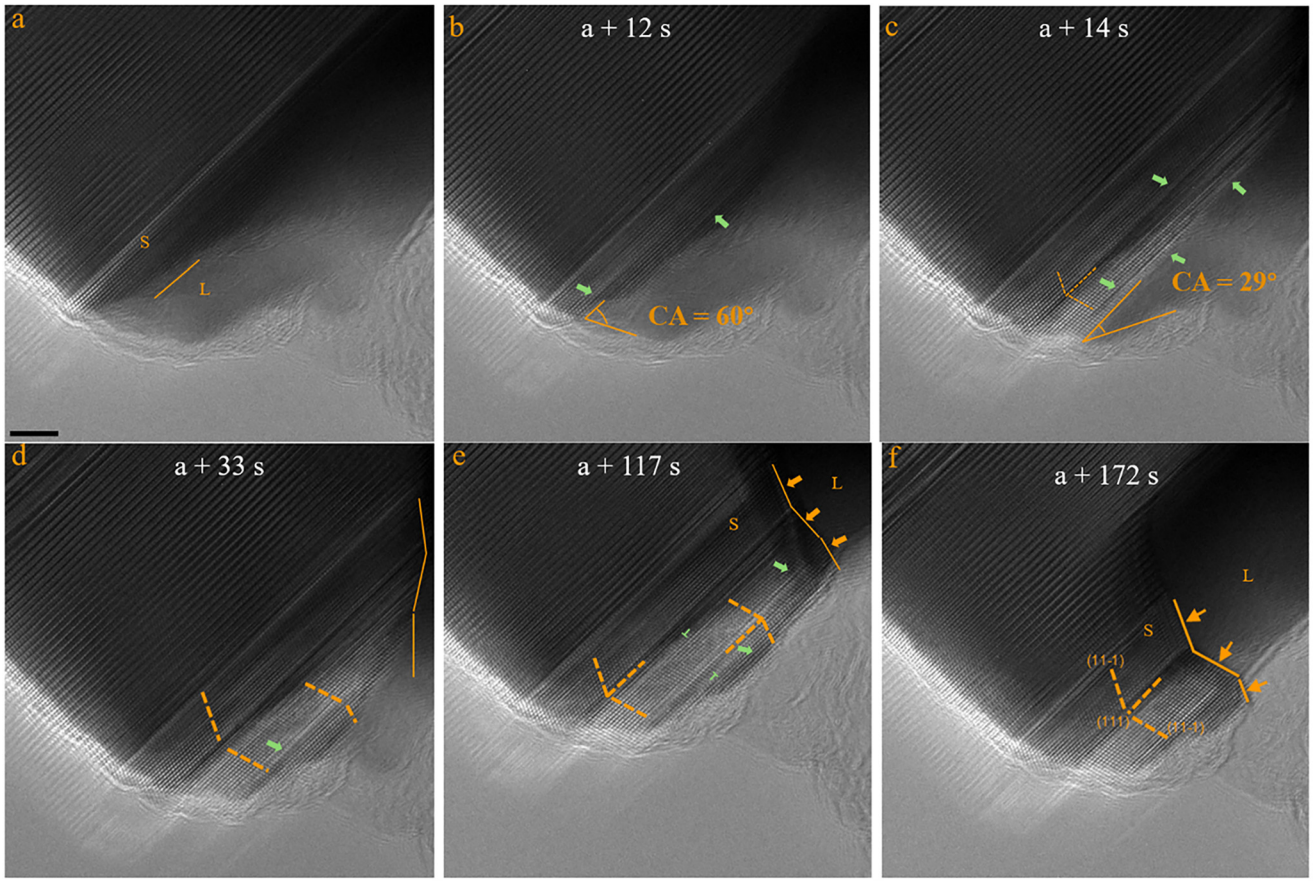

Fig. 4 Oscillatory solidification and liquefaction with the twin superlattice. (a) Initial planar defect-free lattice near the solid–liquid interface. (b) Migration of stacking faults, where the CA is 60 degrees. Green arrows indicate the stacking faults. (c) The process of forming twins, where the CA is 29 degrees. Orange dotted line indicates a {111} twin boundary. (d) Formation of the second {111} twin boundary. (e) Initial liquefaction of the twin superlattice. Orange line indicates the solid–liquid interface, and orange arrows indicate the direction of liquefaction. (f) Liquefaction along the normal direction of twin superlattice growth. Scale bar: 5 nm.

growth mechanism, dictating the structural quality and defect formation in the resulting nanowires.[51] In classical nucleation theory, a distinction is made between homogeneous and heterogeneous nucleation, each governed by different thermodynamic considerations. In homogeneous nucleation, the total free energy change for nucleation is expressed as a function of the nucleus radius:[52,53]

$$\Delta G = \frac{4}{3}\pi r^3 \Delta G_v + 4\pi r^2 \gamma \quad (1)$$

where ΔG_v is the volume free energy change per unit volume and γ is the interfacial energy.

The nucleation barrier in homogeneous nucleation is given by:

$$\Delta G^*_{hom} = \frac{16\pi\gamma^3}{3(\Delta G_v)^2} \quad (2)$$

However, due to the high energy barrier associated with homogeneous nucleation, it is rarely observed under practical growth conditions. In contrast, during heterogeneous nucleation, the presence of a catalyst droplet or a solid surface lowers the nucleation barrier.[54] The presence of a solid surface modifies the shape of the forming nucleus, typically resulting in a spherical cap rather than a complete sphere. This alteration introduces a correction factor that accounts for the influence of the contact angle on nucleation energy:

$$\Delta G^*_{het} = f(\theta)\Delta G^*_{hom} \quad (3)$$

The correction factor, denoted as $f(\theta)$,[55] is a function of the contact angle between the liquid catalyst and the solid surface and can be expressed as:

$$f(\theta) = \frac{(2+\cos\theta)(1-\cos\theta)^2}{4} \quad (4)$$

This function quantifies the extent to which the nucleation barrier is reduced compared to that with homogeneous nucleation. As the contact angle decreases, the correction factor diminishes, leading to a lower energy barrier for nucleation. This relationship has significant implications for the structural integrity of nanowires grown *via* the VLS mechanism.

The impact of the contact angle on nucleation behavior can be analyzed by evaluating the correction factor for various

angles relevant to InAs nanowire solidification. When the contact angle is around 90 degrees, the nucleation energy barrier is reduced by half relative to that with homogeneous nucleation. This configuration promotes controlled nucleation at a single front, minimizing the likelihood of competing nucleation sites and reducing the formation of structural defects. As the contact angle decreases, the nucleation energy barrier becomes progressively lower. At moderate angles like 60 degrees (Fig. 4b), nucleation occurs more readily (correction factor $f(\theta)$ is approximately 0.16); however, the probability of multiple competing nucleation sites increases. This competition can lead to localized lattice distortions, which, in turn, introduce structural imperfections such as dislocations and minor stacking faults. At lower contact angles, particularly below 45 degrees (correction factor $f(\theta)$ is approximately 0.06), the nucleation barrier is significantly diminished, resulting in highly favorable conditions for nucleation (Fig. 3f). Under these conditions, multiple nuclei may form simultaneously at different locations within the catalyst droplet. This uncontrolled nucleation process disrupts the uniformity of the crystal growth front, increasing the probability of twin boundaries and stacking faults. As the contact angle approaches even lower values (below 30 degrees), the nucleation energy barrier is nearly eliminated with the correction factor $f(\theta)$ being approximately 0.01, enabling rapid and widespread nucleation (Fig. 4c). This excessive nucleation leads to a high density of defects, including stacking faults and twinning structures, ultimately compromising the crystallinity of the nanowires. The findings provide a theoretical framework for understanding the relationship between the contact angle and stacking faults and twinning in VLS growth. The analysis of the correction factor demonstrates that maintaining a contact angle close to 90 degrees is optimal for achieving planar defect-free, high-quality nanowires. In contrast, lower contact angles facilitate uncontrolled nucleation, leading to structural imperfections that can degrade the material properties. These results underscore the importance of precise control over the catalyst droplet's wetting behavior to optimize the crystallinity and structural integrity of nanowires. This work not only aligns with experimental observations but also provides a quantitative basis for engineering planar defect-free nanostructures through careful manipulation of growth parameters.

4.2. Dynamic evolution of stacking faults and twinning

Thermally agitated stacking faults exhibit migration along the {111} plane (white box) and the annihilation of stacking faults (orange box) shown in Fig. 5. In essence, the stacking faults

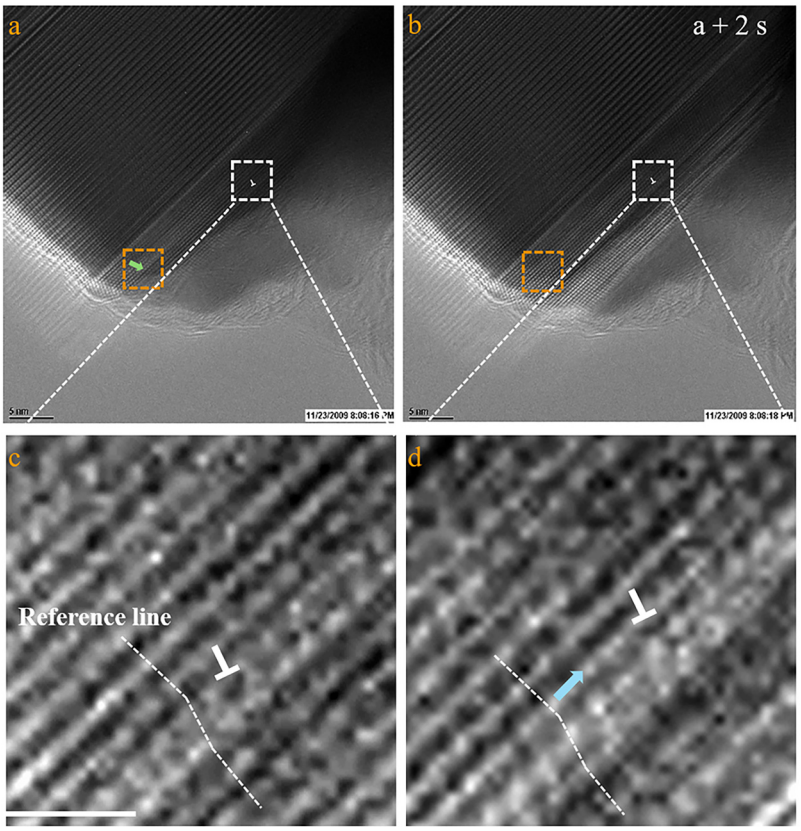

Fig. 5 *In situ* HRTEM observation of the migration of stacking faults along the {111} plane. (a) and (b) Evolution of stacking faults. Orange boxes indicate the annihilation of stacking faults. Green arrow indicates the stacking fault. White boxes indicate the migration of stacking faults. (c) and (d) White boxes in (a) and (b). Blue arrow indicates the slip direction of the dislocation. Scale bar: (a) and (b) 5 nm, (c) and (d) 1 nm.

propagate outward induced by partial dislocation 1/6 ⟨112⟩, perpendicular to the solidification direction, across the nanowire's cross-section. This happens because forming a continuous planar fault across the whole nanowire is energetically favorable compared to a partial fault that would involve additional edge/surface energy at its boundaries. The stacking faults are effectively driven to span the entire crystal cross-section to minimize the energy associated with its edges. As a result, a stacking fault tends to continue across the nanowire diameter, remaining on the same basal plane perpendicular to the solidification direction. Meanwhile, the annihilation of stacking faults also suggests that the system energetically optimizes itself during solidification. Defects that are not energetically favorable tend to be eliminated as atoms arrange into a more stable crystal structure, which aligns with the principle that a growing crystal seeks to minimize its free energy, leading to the removal of high-energy defects. Stacking faults introduce lattice distortions, elevating the crystal free energy. Their migration toward free surfaces allows for the relaxation of these distortions, thereby reducing the system's overall energy. This process is facilitated by surface diffusion mediated by solid–liquid interface fluctuations (contact angle changes), where atoms at or near the surface exhibit increased mobility, enabling the reorganization or elimination of defects to achieve a more stable configuration.

4.3. Liquefaction-induced structural instabilities

In molecular dynamics simulations of face-centered cubic (FCC) metals, the presence of twin interfaces causes liquefaction to occur at a reduced temperature compared to that at the normal melting point.[56] By analogy, but recognizing the different mechanism in III–V ZB semiconductors, in a ZB InAs nanowire, the twin boundary {111} has a lower thermodynamic stability, so when the nanowire is Joule-heated, melting nucleates preferentially along that twin boundary. This defective plane provides an energetically favorable path for the solid-to-liquid transition because fewer bonds must be broken compared to that when melting within the perfect lattice. The system lowers its free energy by melting and dissolving the twin boundary, thereby eliminating the interfacial energy associated with it. Notably, simulations also show that as the temperature approaches the melting point, the twin boundary formation energy drops, meaning the crystal gains little benefit from retaining that twin at high temperature.[56] This drives the selective dissolution of the twin: the nanowire can reduce its total energy by removing the twin plane *via* localized melting. Twin boundaries carry an excess energy (though lower than random grain boundaries, a coherent twin still has a finite energy cost). During biasing, the nanowire's temperature rise, and the twin boundary becomes the weakest link from an energy standpoint. Liquefaction concentrates at the twin boundary to minimize energy, effectively "peeling apart" the twin. Removing the twin plane erases its defect energy, yielding a more stable single-crystalline region. This is analogous to how chemical etching or oxidation often proceeds preferentially at defect sites—here, thermally driven liquefaction preferentially nucleates along the twin boundary. The result is a selective dissolution of the twin interface: the twin plane melts before the rest of the lattice, creating a liquid layer along that plane. This behavior is an outcome of energy minimization principles; the system favors a state without a high-energy interface. In short, the twin boundary elevated energy density makes it a hotspot for a phase change, explaining why liquefaction occurs preferentially along the twin plane. Once a thin liquid layer nucleates at the twin plane, a solid–liquid interface is established between the remaining crystal and the molten

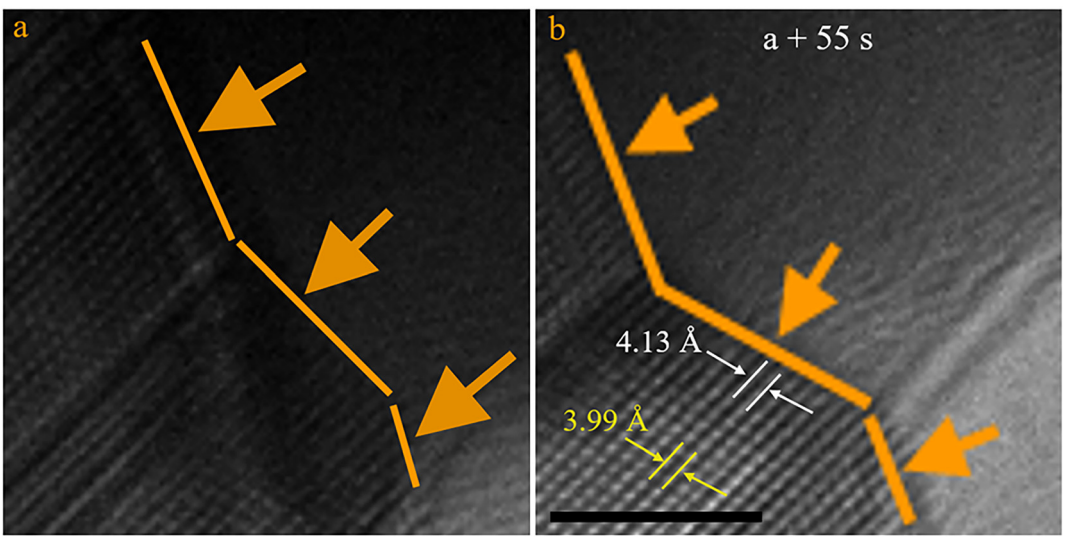

Fig. 6 *In situ* HRTEM observation of the solid–liquid interface during the liquefaction process. (a) The interface of solid to liquid transformation. The orange arrows represent the liquefaction direction. (b) Different interplanar spacing of the interface (white) and twinning plane (yellow). Scale bar: 5 nm. (a) and (b) The magnification of the melting front in Fig. 4(e) and (f).

region. Observations indicate that this interface migrates along the plane of the twin, rather than arbitrarily through the crystal lattice. This behavior can be understood by considering interface energetics and the pre-existing structural pathway. The twin boundary is a ready-made two-dimensional defect plane that the liquid can spread along with minimal resistance. In crystallographic terms, the twin plane in zinc blende InAs is typically a {111} plane – a close-packed plane. A liquid–solid interface that lies on a low-index plane tends to have a lower interfacial free energy, which makes it more stable and likely to propagate in-plane rather than break into the perfect lattice. In other words, the melting front locks onto the twin boundary plane because that orientation minimizes the interface energy. Breaking into the undisturbed lattice (off the twin plane) would require creating a new interface with higher energy (since the crystal is coherent and planar defect-free away from the twin), so the system avoids that. Instead, the melt front extends along the twin, melting away the defect plane like a zipper unzipping. This results in the interface moving in a controlled manner aligned with the twin boundary. Such planar interface migration is reminiscent of one of the known nanowire liquefaction modes identified in simulations: a stable melt interface that advances steadily rather than an unstable breakup.[57] Furthermore, Fig. 6 reveals that the interplanar spacing (*d*-spacing) at the solid–liquid interface is larger than that in the twin planes away from the interface. This expansion can be attributed to the presence of a premelting layer, where a quasi-liquid region forms before complete melting, resulting in structural disorder and increased interatomic distances.[58,59] Additionally, strain accumulation at the interface due to twin boundary constraints may contribute to local dilation. The observed interface expansion suggests that the melting front is not an abrupt transition but rather involves a gradual atomic rearrangement influenced by thermodynamic and kinetic factors. This reinforces the idea that the liquefaction process at twin boundaries follows an energetically favorable pathway, driven by interface-induced instabilities and pre-existing structural features that guide the solid–liquid transformation.[60]

5. Conclusion

Using *in situ* HRTEM, the dynamic evolution of stacking faults and twinning in semiconductor InAs was directly observed. First, the results indicate that the formation of stacking faults and twins arises from fluctuations in the contact angle at the solid–liquid interface. Specifically, as the contact angle decreases, the nucleation energy barrier is substantially reduced, resulting in an increased density of stacking faults and twins. This process is closely associated with interfacial energetics, whereby a lower contact angle facilitates heterogeneous nucleation. Second, thermally activated stacking faults were observed to migrate along the {111} planes and undergo annihilation. The migration is mediated by partial dislocations, while annihilation is driven by fluctuations at the solid–liquid interface that reflect the system's tendency toward energy minimization. These fluctuations enhance atomic surface diffusivity, enabling self-correction and the elimination of stacking faults. Third, the liquefaction of InAs is accompanied by twin dissociation at the twin boundaries. The twin plane acts as a low-energy pathway for the liquid–solid transition, guiding the melting front along a structurally favorable direction. This behavior highlights the significance of interfacial energy minimization in defect-mediated liquid–solid phase transitions.

Collectively, these atomic-scale observations provide important insights into the nucleation-driven mechanisms that control stacking fault and twinning evolution during solidification. Understanding these defect dynamics allows for better control of phase stability and defects in semiconductors. By adjusting growth conditions—such as the solid–liquid contact angle and catalyst composition—the defect structure can be tuned to improve the electronic and optoelectronic properties of nanowires. These findings provide a basis for the design of defect-engineered semiconductors, with broad potential for applications in quantum transport devices, infrared photodetectors, and high-speed nanoelectronics.

Author contributions

Changxin Han: writing – original draft, writing – review & editing, investigation, formal analysis, and conceptualization. Bohua Zhang: investigation. He Zheng: data curation. Scott X. Mao: supervision, resources, and project administration.

Conflicts of interest

The authors declare that they have no known competing financial interests or personal relationships that could have appeared to influence the work reported in this paper.

Data availability

All data collected within this research are reported in the main text of the article and in its supplementary information (SI). Supplementary information is available (experiment video and additional data on the characterization of InAs). See DOI: https://doi.org/10.1039/d5nr02745d.

Acknowledgements

S. M. would like to acknowledge NSF DMR 1808046 through the University of Pittsburgh. This work was performed, in part, at the Center for Integrated Nanotechnologies, a U.S. Department of Energy, Office of Basic Energy Sciences user facility. Sandia National Laboratories is a multiprogram laboratory operated by Sandia Corporation, a Lockheed-Martin

Company, for the U.S. Department of Energy under Contract No. DE-AC04-94AL85000.

References

1 M. S. Gudiksen, L. J. Lauhon, J. Wang, D. C. Smith and C. M. Lieber, Growth of Nanowire Superlattice Structures for Nanoscale Photonics and Electronics, *Nature*, 2002, **415**(6872), 617–620, DOI: 10.1038/415617a.

2 K. A. Dick, K. Deppert, M. W. Larsson, T. Mårtensson, W. Seifert, L. R. Wallenberg and L. Samuelson, Synthesis of Branched "nanotrees" by Controlled Seeding of Multiple Branching Events, *Nat. Mater.*, 2004, **3**(6), 380–384, DOI: 10.1038/nmat1133.

3 A. I. Hochbaum, R. Chen, R. D. Delgado, W. Liang, E. C. Garnett, M. Najarian, A. Majumdar and P. Yang, Enhanced Thermoelectric Performance of Rough Silicon Nanowires, *Nature*, 2008, **451**(7175), 163–167, DOI: 10.1038/nature06381.

4 J. A. Van Dam, Y. V. Nazarov, E. P. A. M. Bakkers, S. De Franceschi and L. P. Kouwenhoven, Supercurrent Reversal in Quantum Dots, *Nature*, 2006, **442**(7103), 667–670, DOI: 10.1038/nature05018.

5 Z. Zhang, N. Liu, L. Li, J. Su, P.-P. Chen, W. Lu, Y. Gao and J. Zou, In Situ TEM Observation of Crystal Structure Transformation in InAs Nanowires on Atomic Scale, *Nano Lett.*, 2018, **18**(10), 6597–6603, DOI: 10.1021/acs.nanolett.8b03231.

6 H. Zheng, J. Wang, J. Y. Huang, J. Wang, Z. Zhang and S. X. Mao, Dynamic Process of Phase Transition from Wurtzite to Zinc Blende Structure in InAs Nanowires, *Nano Lett.*, 2013, **13**(12), 6023–6027, DOI: 10.1021/nl403240r.

7 H. Tsuzuki, D. F. Cesar, M. Rebello Sousa Dias, L. K. Castelano, V. Lopez-Richard, J. P. Rino and G. E. Marques, Tailoring Electronic Transparency of Twin-Plane 1D Superlattices, *ACS Nano*, 2011, **5**(7), 5519–5525, DOI: 10.1021/nn2008589.

8 S. M. Sze and K. K. Ng, in *Physics of Semiconductor Devices*, Wiley, 1st edn, 2006. DOI: 10.1002/0470068329.

9 C. Thelander, P. Agarwal, S. Brongersma, J. Eymery, L. F. Feiner, A. Forchel, M. Scheffler, W. Riess, B. J. Ohlsson, U. Gösele and L. Samuelson, Nanowire-Based One-Dimensional Electronics, *Mater. Today*, 2006, **9**(10), 28–35, DOI: 10.1016/S1369-7021(06)71651-0.

10 D. T. J. Hurle and P. Rudolph, A Brief History of Defect Formation, Segregation, Faceting, and Twinning in Melt-Grown Semiconductors, *J. Cryst. Growth*, 2004, **264**(4), 550–564, DOI: 10.1016/j.jcrysgro.2003.12.035.

11 T. Akiyama, K. Nakamura and T. Ito, Effects of Surface and Twinning Energies on Twining-Superlattice Formation in Group III–V Semiconductor Nanowires: A First-Principles Study, *Nanotechnology*, 2019, **30**(23), 234002, DOI: 10.1088/1361-6528/ab06d0.

12 T. P. Chen, F. R. Chen, Y. C. Chuang, Y. D. Guo, J. G. Peng, T. S. Huang and L. J. Chen, Study of Twins in GaAs, GaP and InAs Crystals, *J. Cryst. Growth*, 1992, **118**(1–2), 109–116, DOI: 10.1016/0022-0248(92)90055-N.

13 J. Johansson, L. S. Karlsson, T. Patrik, C. Svensson, T. Mårtensson, B. A. Wacaser, K. Deppert, L. Samuelson and W. Seifert, Structural Properties of ⟨111⟩ B -Oriented III–V Nanowires, *Nat. Mater.*, 2006, **5**(7), 574–580, DOI: 10.1038/nmat1677.

14 F. Wang and W. E. Buhro, Surfactant-Mediated Solution-Liquid–Solid (SLS) Growth of Phase-Pure Wurtzite CdS Quantum Wires, *Chem. Mater.*, 2024, **36**(20), 10307–10318, DOI: 10.1021/acs.chemmater.4c02283.

15 C. Jia, Z. Lin, Y. Huang and X. Duan, Nanowire Electronics: From Nanoscale to Macroscale, *Chem. Rev.*, 2019, **119**(15), 9074–9135, DOI: 10.1021/acs.chemrev.9b00164.

16 P. Krogstrup, R. Popovitz-Biro, E. Johnson, M. H. Madsen, J. Nygård and H. Shtrikman, Structural Phase Control in Self-Catalyzed Growth of GaAs Nanowires on Silicon (111), *Nano Lett.*, 2010, **10**(11), 4475–4482, DOI: 10.1021/nl102308k.

17 K. Ikejiri, Y. Kitauchi, K. Tomioka, J. Motohisa and T. Fukui, Correction to Zinc Blende and Wurtzite Crystal Phase Mixing and Transition in Indium Phosphide Nanowires, *Nano Lett.*, 2012, **12**(1), 524–525, DOI: 10.1021/nl2042886.

18 E. Husanu, D. Ercolani, M. Gemmi and L. Sorba, Growth of Defect-Free GaP Nanowires, *Nanotechnology*, 2014, **25**(20), 205601, DOI: 10.1088/0957-4484/25/20/205601.

19 M. Koguchi, H. Kakibayashi, M. Yazawa, K. Hiruma and T. Katsuyama, Crystal Structure Change of GaAs and InAs Whiskers from Zinc-Blende to Wurtzite Type, *Jpn. J. Appl. Phys.*, 1992, **31**(7R), 2061, DOI: 10.1143/JJAP.31.2061.

20 J. Johansson, K. A. Dick, P. Caroff, M. E. Messing, J. Bolinsson, K. Deppert and L. Samuelson, Diameter Dependence of the Wurtzite–Zinc Blende Transition in InAs Nanowires, *J. Phys. Chem. C*, 2010, **114**(9), 3837–3842, DOI: 10.1021/jp910821e.

21 P. Caroff, K. A. Dick, J. Johansson, M. E. Messing, K. Deppert and L. Samuelson, Controlled Polytypic and Twin-Plane Superlattices in Iii–v Nanowires, *Nat. Nanotechnol.*, 2009, **4**(1), 50–55, DOI: 10.1038/nnano.2008.359.

22 F. M. Davidson, D. C. Lee, D. D. Fanfair and B. A. Korgel, Lamellar Twinning in Semiconductor Nanowires, *J. Phys. Chem. C*, 2007, **111**(7), 2929–2935, DOI: 10.1021/jp0672205.

23 Z. Liu, I. Papadimitriou, M. Castillo-Rodríguez, C. Wang, G. Esteban-Manzanares, X. Yuan, H. H. Tan, J. M. Molina-Aldareguía and J. Llorca, Mechanical Behavior of InP Twinning Superlattice Nanowires, *Nano Lett.*, 2019, **19**(7), 4490–4497, DOI: 10.1021/acs.nanolett.9b01300.

24 M. T. Soo, K. Zheng, Q. Gao, H. H. Tan, C. Jagadish and J. Zou, Mirror-Twin Induced Bicrystalline InAs Nanoleaves, *Nano Res.*, 2016, **9**(3), 766–773, DOI: 10.1007/s12274-015-0955-z.

25 M. J. L. Sourribes, I. Isakov, M. Panfilova, H. Liu and P. A. Warburton, Mobility Enhancement by Sb-Mediated Minimisation of Stacking Fault Density in InAs Nanowires

Grown on Silicon, *Nano Lett.*, 2014, **14**(3), 1643–1650, DOI: 10.1021/nl5001554.

26 S. A. Dayeh, W. Tang, F. Boioli, K. L. Kavanagh, H. Zheng, J. Wang, N. H. Mack, G. Swadener, J. Y. Huang, L. Miglio, K.-N. Tu and S. T. Picraux, Direct Measurement of Coherency Limits for Strain Relaxation in Heteroepitaxial Core/Shell Nanowires, *Nano Lett.*, 2013, **13**(5), 1869–1876, DOI: 10.1021/nl3022434.

27 A. D. Gamalski, J. Tersoff and E. A. Stach, Atomic Resolution in Situ Imaging of a Double-Bilayer Multistep Growth Mode in Gallium Nitride Nanowires, *Nano Lett.*, 2016, **16**(4), 2283–2288, DOI: 10.1021/acs.nanolett.5b04650.

28 J. Bao, D. C. Bell, F. Capasso, J. B. Wagner, T. Mårtensson, J. Trägårdh and L. Samuelson, Optical Properties of Rotationally Twinned InP Nanowire Heterostructures, *Nano Lett.*, 2008, **8**(3), 836–841, DOI: 10.1021/nl072921e.

29 Z. Ikonic, G. P. Srivastava and J. C. Inkson, Optical Properties of Twinning Superlattices in Diamond-Type and Zinc-Blende-Type Semiconductors, *Phys. Rev. B: Condens. Matter Mater. Phys.*, 1995, **52**(19), 14078–14085, DOI: 10.1103/PhysRevB.52.14078.

30 S. Kodambaka, J. Tersoff, M. C. Reuter and F. M. Ross, Germanium Nanowire Growth Below the Eutectic Temperature, *Science*, 2007, **316**(5825), 729–732, DOI: 10.1126/science.1139105.

31 Q. Sun, D. Pan, M. Li, J. Zhao, P. Chen, W. Lu and J. Zou, *In Situ* TEM Observation of the Vapor–Solid–Solid Growth of InAs Nanowires, *Nanoscale*, 2020, **12**(21), 11711–11717, DOI: 10.1039/D0NR02892D.

32 L. Zhong, J. Wang, H. Sheng, Z. Zhang and S. X. Mao, Formation of Monatomic Metallic Glasses through Ultrafast Liquid Quenching, *Nature*, 2014, **512**(7513), 177–180, DOI: 10.1038/nature13617.

33 L. Wang, T. Xin, D. Kong, X. Shu, Y. Chen, H. Zhou, J. Teng, Z. Zhang, J. Zou and X. Han, In Situ Observation of Stress Induced Grain Boundary Migration in Nanocrystalline Gold, *Scr. Mater.*, 2017, **134**, 95–99, DOI: 10.1016/j.scriptamat.2017.03.003.

34 F. Lenrick, M. Ek, K. Deppert, L. Samuelson and L. R. Wallenberg, Straight and Kinked InAs Nanowire Growth Observed in Situ by Transmission Electron Microscopy, *Nano Res.*, 2014, **7**(8), 1188–1194, DOI: 10.1007/s12274-014-0481-4.

35 H. Xu, Y. Wang, Y. Guo, Z. Liao, Q. Gao, H. H. Tan, C. Jagadish and J. Zou, Defect-Free Zinc-Blende Structured InAs Nanowires Catalyzed by Palladium, *Nano Lett.*, 2012, **12**(11), 5744–5749, DOI: 10.1021/nl303028u.

36 D. Jacobsson, F. Panciera, J. Tersoff, M. C. Reuter, S. Lehmann, S. Hofmann, K. A. Dick and F. M. Ross, Interface Dynamics and Crystal Phase Switching in GaAs Nanowires, *Nature*, 2016, **531**(7594), 317–322, DOI: 10.1038/nature17148.

37 S. E. H. Amiri, S. Turkdogan, P. Ranga, F. Fan, L. Gan and C.-Z. Ning, Vapor–Liquid–Solid Growth of Highly Stoichiometric Gallium Phosphide Nanowires on Silicon: Restoration of Chemical Balance, Congruent Sublimation and Maximization of Band-Edge Emission, *Eur. Phys. J.: Spec. Top.*, 2022, **231**(4), 723–734, DOI: 10.1140/epjs/s11734-021-00388-3.

38 R. E. Algra, M. A. Verheijen, M. T. Borgström, L.-F. Feiner, G. Immink, W. J. P. Van Enckevort, E. Vlieg and E. P. A. M. Bakkers, Twinning Superlattices in Indium Phosphide Nanowires, *Nature*, 2008, **456**(7220), 369–372, DOI: 10.1038/nature07570.

39 S. A. Dayeh, D. Susac, K. L. Kavanagh, E. T. Yu and D. Wang, Structural and Room–Temperature Transport Properties of Zinc Blende and Wurtzite InAs Nanowires, *Adv. Funct. Mater.*, 2009, **19**(13), 2102–2108, DOI: 10.1002/adfm.200801307.

40 S. A. Dayeh, E. T. Yu and D. Wang, III–V Nanowire Growth Mechanism: V/III Ratio and Temperature Effects, *Nano Lett.*, 2007, **7**(8), 2486–2490, DOI: 10.1021/nl0712668.

41 H. Zheng, A. Cao, C. R. Weinberger, J. Y. Huang, K. Du, J. Wang, Y. Ma, Y. Xia and S. X. Mao, Discrete Plasticity in Sub-10-Nm-Sized Gold Crystals, *Nat. Commun.*, 2010, **1**(1), 144, DOI: 10.1038/ncomms1149.

42 H. Zheng, J. Wang, J. Y. Huang, A. Cao and S. X. Mao, *In Situ* Visualization of Birth and Annihilation of Grain Boundaries in an Au Nanocrystal, *Phys. Rev. Lett.*, 2012, **109**(22), 225501, DOI: 10.1103/PhysRevLett.109.225501.

43 Y. He, L. Zhong, F. Fan, C. Wang, T. Zhu and S. X. Mao, In Situ Observation of Shear-Driven Amorphization in Silicon Crystals, *Nat. Nanotechnol.*, 2016, **11**(10), 866–871, DOI: 10.1038/nnano.2016.166.

44 L. Güniat, P. Caroff and A. Fontcuberta i Morral, Vapor Phase Growth of Semiconductor Nanowires: Key Developments and Open Questions, *Chem. Rev.*, 2019, **119**(15), 8958–8971, DOI: 10.1021/acs.chemrev.8b00649.

45 M. Song, Y. Zhang, J. Chun, S. Hu, M. Tang and D. Li, Effects of Catalyst Droplets on Wire Growth and the Resulting Branched Structures during VLS Growth, *Nanoscale*, 2020, **12**(14), 7538–7543, DOI: 10.1039/C9NR10695B.

46 B. A. Wacaser, K. A. Dick, J. Johansson, M. T. Borgström, K. Deppert and L. Samuelson, Preferential Interface Nucleation: An Expansion of the VLS Growth Mechanism for Nanowires, *Adv. Mater.*, 2009, **21**(2), 153–165, DOI: 10.1002/adma.200800440.

47 M. Tornberg, R. Sjökvist, K. Kumar, C. R. Andersen, C. B. Maliakkal, D. Jacobsson and K. A. Dick, Direct Observations of Twin Formation Dynamics in Binary Semiconductors, *ACS Nanosci. Au*, 2022, **2**(1), 49–56, DOI: 10.1021/acsnanoscienceau.1c00021.

48 T. Zhou, *In Situ Synchrotron X-Ray Scattering of SiGe NWs: Growth, Strain and Bending*, Thesis, Université Grenoble Alpes, 2015.

49 J. Li and F. L. Deepak, *In Situ* Kinetic Observations on Crystal Nucleation and Growth, *Chem. Rev.*, 2022, **122**(23), 16911–16982, DOI: 10.1021/acs.chemrev.1c01067.

50 M. A. Boles, M. Engel and D. V. Talapin, Self-Assembly of Colloidal Nanocrystals: From Intricate Structures to Functional Materials, *Chem. Rev.*, 2016, **116**(18), 11220–11289, DOI: 10.1021/acs.chemrev.6b00196.

51 B. Mandl, J. Stangl, E. Hilner, A. A. Zakharov, K. Hillerich, A. W. Dey, L. Samuelson, G. Bauer, K. Deppert and A. Mikkelsen, Growth Mechanism of Self-Catalyzed Group III–V Nanowires, *Nano Lett.*, 2010, **10**(11), 4443–4449, DOI: 10.1021/nl1022699.
52 R. P. Sear, Nucleation: Theory and Applications to Protein Solutions and Colloidal Suspensions, *J. Phys.: Condens. Matter*, 2007, **19**(3), 033101, DOI: 10.1088/0953-8984/19/3/033101.
53 F. F. Abraham and A. C. Zettlemoyer, Homogeneous Nucleation Theory, *Phys. Today*, 1974, **27**(12), 52–53, DOI: 10.1063/1.3129038.
54 X. Y. Liu, Heterogeneous Nucleation or Homogeneous Nucleation?, *J. Chem. Phys.*, 2000, **112**(22), 9949–9955, DOI: 10.1063/1.481644.
55 C. A. Sholl and N. H. Fletcher, Decoration Criteria for Surface Steps, *Acta Metall.*, 1970, **18**(10), 1083–1086, DOI: 10.1016/0001-6160(70)90006-4.
56 S. S. Hayat, M. A. Choudhry and S. A. Ahmad, Effect of Twin-Boundaries on Melting of Aluminum, *J. Mater. Sci.*, 2008, **43**(14), 4915–4920, DOI: 10.1007/s10853-008-2715-x.
57 K. M. Ridings and S. C. Hendy, Nanowire Melting Modes during the Solid–Liquid Phase Transition: Theory and Molecular Dynamics Simulations, *Sci. Rep.*, 2022, **12**(1), 20052, DOI: 10.1038/s41598-022-24654-z.
58 J. Luo, Stabilization of Nanoscale Quasi-Liquid Interfacial Films in Inorganic Materials: A Review and Critical Assessment, *Crit. Rev. Solid State Mater. Sci.*, 2007, **32**(1–2), 67–109, DOI: 10.1080/10408430701364388.
59 J. G. Dash, H. Fu and J. S. Wettlaufer, The Premelting of Ice and Its Environmental Consequences, *Rep. Prog. Phys.*, 1995, **58**(1), 115–167, DOI: 10.1088/0034-4885/58/1/003.
60 K. Fujiwara, M. Tokairin, W. Pan, H. Koizumi, J. Nozawa and S. Uda, Instability of Crystal/Melt Interface Including Twin Boundaries of Silicon, *Appl. Phys. Lett.*, 2014, **104**(18), 182110, DOI: 10.1063/1.4876177.